



POLITECNICO
MILANO 1863

SCUOLA DI INGEGNERIA INDUSTRIALE
E DELL'INFORMAZIONE



BUMP - BUbbly column Multiphase Project

Stefano Passoni, Martina Di Gennaro, Riccardo Giordani

Contents

1	Introduction	2
2	Experimental Benchmark	2
3	Numerical Setup	2
3.1	Domain and Mesh	3
3.2	Boundary Conditions	4
3.3	Working fluids and operating conditions	4
3.4	Turbulence modeling	5
3.4.1	$k - \omega$ SST Sato	5
3.4.2	Lahey $k - \epsilon$	6
3.4.3	Mixture $k - \epsilon$	6
3.5	Solver settings	7
3.6	Phase interaction modeling	8
3.6.1	Virtual mass force	8
3.6.2	Drag force	8
3.6.3	Lift force	8
3.6.4	Turbulent dispersion	9
3.6.5	Wall lubrication	9
4	Results and Discussion	10
4.1	CFD methodology	10
4.2	Mesh sensitivity	10
4.3	Time sensitivity	12
4.4	Turbulence models	12
4.5	Drag models	13
4.6	Lift models	13
4.7	Turbulent dispersion models	14
4.8	Wall lubrication models	15
4.9	Inflow velocity	15
A	Appendix A: fvModels source code for degassing boundary conditions	17

1. Introduction

Bubble columns are multiphase reactors where the dispersed phase (gas) is introduced into a stationary or flowing liquid (continuous phase) and provide a good experimental setup to study the turbulent phenomena in dense bubbly flows. The functioning is apparently simple, as the ascending gas-phase creates a buoyancy-driven flow inducing the recirculation of the liquid phase. The local and the global fluid dynamic properties are related to the prevailing flow regime which may be homogeneous (bubbly flow condition at low superficial gas velocity, typically $U_G < 0.03 \text{ m/s}$) or heterogeneous (churn-turbulent flow condition, $U_G > 0.1 \text{ m/s}$, $\alpha_G \geq 0.3$). The homogeneous flow regime can be classified into the *mono-dispersed homogeneous* flow regime, characterized by a mono-dispersed bubble size distribution (BSD), and the *pseudo-homogeneous* flow regime, characterized by a poly-dispersed BSD. The distinction between mono-dispersed and poly-dispersed BSDs is based upon the change in the sign of the lift force coefficient.

Numerous industrial designs have been based on empirical correlations, but such approaches remain somewhat limited when increasing the reactor performance is sought. To improve the description of the physical phenomenon occurring in bubble columns a promising numerical method is the Computational Fluid Dynamics (CFD). CFD helps to understand the complex two-phase fluid dynamics in the bubble column through details of mean flows (fields of three components of mean velocities and mean gas hold-up), interphase rates of mass, energy and momentum transfer and turbulence parameters (such as turbulent kinetic energy, energy dissipation rate, Reynolds stresses, etc.).

In the present work, bubble column is numerically simulated by using the open source CFD tool OpenFOAM [1]. More in detail, the objective of this work is the validation of the already existing *multiphaseEulerFoam* solver working for the case of *mono-dispersed homogeneous* bubble column. For the case study we have considered a multiphase mixture of air and water without taking into account the heat transfer phenomena.

The structure of the report is as follows. In Section 2, the experimental benchmark taken as reference is illustrated. In Section 3, all details related to the numerical setup are delineated. In Section 4, the results are discussed. Conclusions and further development are outlined in Section 5.

2. Experimental Benchmark

The experimental benchmark taken as reference for the validation comes from the literature, in particular from the study of Krepper et al. [2]. The experimental setup consists of three rectangular channels 20cm^2 in cross-section ($0.1 \times 0.02 \text{ m}$) bolted together at the flanges resulting in a bubble column of 1-meter height (Figure 1). The test facility is initially filled with water up to a specified (..) height. In the bottom of the test section is present a rectangular porous stone adopted as gas sparger 0.02m wide, 0.01m depth and 0.01m height. This sparger produced a *mono-dispersed homogeneous* bubble size distribution with a bubble diameter of 3-5 mm. The superficial gas flow rate, U_G , is varied between three different value, 0.006 m/s , 0.008 m/s and 0.010 m/s , in the *mono-dispersed homogeneous* flow regime. The superficial velocity is calculated from the measured volume flow rates using:

$$U_G = \frac{Q_G}{A_{CS}} \quad (1)$$

where Q_G is the measured volume flow rate of the gas and A_{CS} is the cross-sectional area of the test section. The column operates in the dispersed bubble bubbly regime, characterized by the absence of bubble coalescence or breakup, for the superficial gas velocities adopted in this work. For each superficial gas velocity the volume average void fraction, α_V , also known as *gas holdup*, can be calculated using:

$$\alpha_V = \frac{h_{final} - h_{initial}}{h_{final}} \quad (2)$$

where h_{final} is the height of the liquid column after the column has been aerated and $h_{initial}$ is the stationary height of the liquid column before aeration. The experimental data consist of wire-mesh local void fraction measurements performed at two different axial heights $y = 0.08 \text{ m}$ and $y = 0.63 \text{ m}$ above the gas sparger). The wire mesh sensor is placed in the cross-section by bolting it to two flanged rectangular channels. The wire-mesh sensor data was recorded at a frequency of 2500 Hz for a time period of 60 s.

3. Numerical Setup

In this section all the details related to the numerical setup will be presented and discussed.

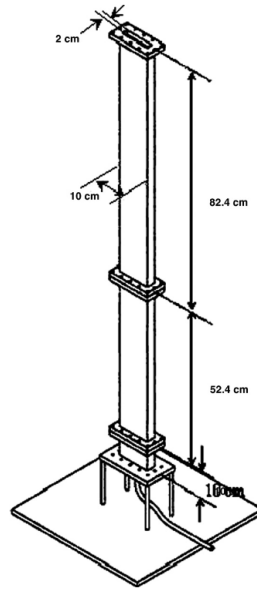


Figure 1: Dimensions and geometry of the experimental test facility.

3.1. Domain and Mesh

The numerical domain has been modeled and meshed with the utility **blockMesh** according to the size of the experimental facility reported in section 2. The resulting mesh is structured and made of only regular hexahedral elements. Four different refinement levels were analyzed for the purpose of a grid sensitivity analysis. Figure 2 displays a section of the generated meshes and their details are instead summarized in table 1. According to [2], the mesh size should be 1.5 times the size of the bubbles. Therefore, given the size distribution found in the experiments (see section 2), the coarsest mesh should be the most adequate since it has a cell size of 5mm in each direction. The grid refinement study has the purpose of verify if such a coarse mesh has negative influence on the fluid-dynamic phenomena inside the bubble column.

Speaking about the inlet section, the porous stone used as gas sparger in the experiments has been modeled as a zero-thickness surface having the size of the sparger itself, namely a $0.02 \times 0.01 \text{ m}^2$ cross-section.

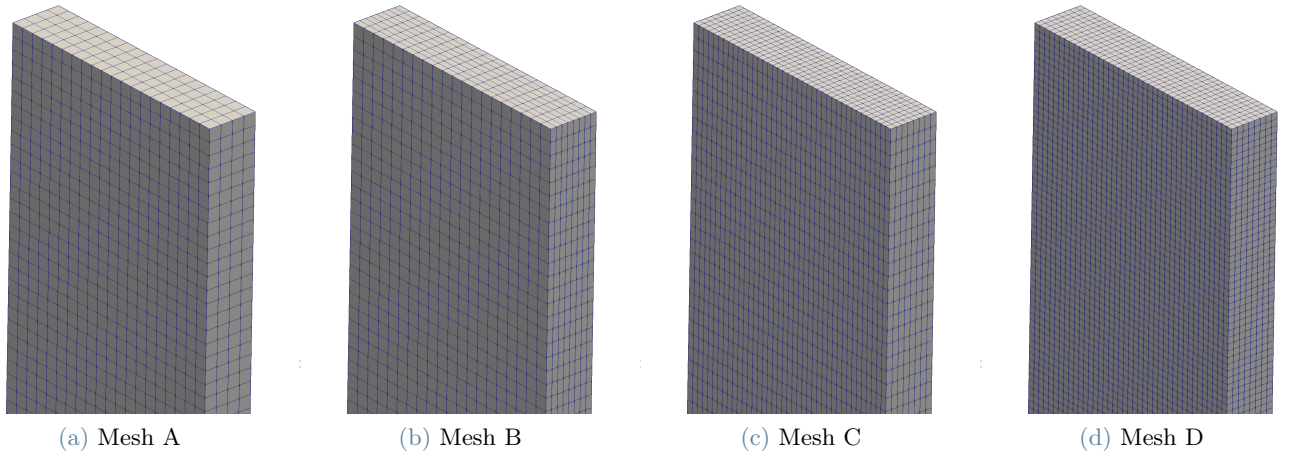


Figure 2: Different mesh densities considered in the analysis

	N_x	N_y	N_z	Total no. of elements
Mesh A	20	200	4	16000
Mesh B	20	200	8	32000
Mesh C	40	200	8	64000
Mesh D	40	400	8	128000

Table 1: Mesh size details

3.2. Boundary Conditions

The list of boundary conditions applied to the domain is summarized in table 2. At the inlet, three different gas superficial velocities were applied according to the three cases studied, respectively 6, 8 and 10 mm/s. These superficial velocities are an experimental input and were calculated as the volumetric flow rate of gas injected in the column divided by its volume. In OpenFOAM, a `flowRateInletVelocity` boundary condition was employed. This requires a mass flow rate input and a reference density in order to calculate the inlet velocity. The chosen density was 1.185 kg/m³ which corresponds to air density at ambient conditions of 25°C and 1 atm.

Moreover, a custom `fvModels` boundary condition was developed to implement a degassing boundary condition. The complete listing of the source code is provided in Appendix A. Typically, a this type boundary condition is used to model a free surface through which dispersed gas bubbles are allowed to escape, but the continuous phase is not. A typical application is a bubble column in which the user want to reduce computational cost by not including the freeboard region in the simulation [3]. This boundary conditions offers also an improvement in terms of numerical stability since the water-air interface is not modeled. When the degassing boundary condition is specified for an outlet, the continuous liquid phase sees the boundary as a free-slip wall and does not leave the domain. The dispersed gas phase sees the boundary as an outlet. The code provided calculates an implicit mass source term to remove gas phase from the cells adjacent to the outlet boundary and also computes a degassing force to account for the effect of gas removal on the continuous phase. By adding the degassing boundary condition, the gas holdup of the entire bubble column can be simply calculated as the void fraction of air in the entire domain.

Variable	Inlet	Outlet	Walls
alpha.air	fixedValue	zeroGradient	zeroGradient
alpha.water	fixedValue	zeroGradient	zeroGradient
k.water	fixedValue	inletOutlet	kqRWallFunction
epsilon.water	fixedValue	inletOutlet	epsilonWallFunction
omega.water	fixedValue	inletOutlet	omegaWallFunction
km	fixedValue	inletOutlet	kqRWallFunction
epsilon _{nm}	fixedValue	inletOutlet	epsilonWallFunction
nut.water	calculated	calculated	nutkWallFunction
p	calculated	calculated	calculated
U.air	flowRateInletVelocity	pressureInletOutletVelocity	fixedValue
U.water	fixedValue	slip	fixedValue

Table 2: List of boundary conditions applied to the three different boundaries

3.3. Working fluids and operating conditions

In order to model the bubble column, a two-phase mixture made of air and water was considered. As reported in section 2, the experimental setup provided a monodispersed bubble size distribution with a mean equivalent diameter of 3mm. The dispersed phase is therefore modeled by using a single gas phase considering only small

bubbles. Despite the air phase having a slightly varying density from the bottom to the top of the column, both fluids are considered incompressible. Table 3 summarizes material properties of both phases. The column was simulated at ambient pressure of 10^5 Pa with gravitational acceleration acting along Z coordinate. The system was considered isothermal and no thermophysical property was dependent on temperature. No heat nor mass transfer was considered between phases.

Phase	Property	Type	Value
Air	Density	Constant	1.185 [kg/m ³]
Water	Density	Constant	998.0 [kg/m ³]
Air	Bubble diameter	Constant	3 [mm]
Air and water	Surface Tension	Constant	0.072 [N/m]
Air	Eötvös number	Constant	1
Air	Dynamic viscosity	Constant	1.84e-05 [Pa/s]
Water	Dynamic viscosity	Constant	3.65e-04 [Pa/s]

Table 3: List of boundary conditions applied to the three different boundaries

3.4. Turbulence modeling

3.4.1 $k - \omega$ SST Sato

The $k - \omega$ SST Sato model [4] has originally developed to tackle the problem of heat transfer for boundary layer flows. It combines eddy-viscosity models for the momentum equations and eddy-diffusivity model for heat transfer.

The idea behind SST model is to combine the best elements of the $k - \epsilon$ model and the $k - \omega$ model with the help of a blending function. Indeed, the $k - \epsilon$ model presents deficiencies near the wall, where fine meshes and specific near-wall treatments are required. Whereas, the $k - \omega$ model is strongly dependent of the solution to free stream values of ω outside the boundary layer.

The turbulent model equations reads:

$$\frac{\partial \rho k}{\partial t} + \frac{\partial \rho U_j k}{\partial x_j} = \tilde{P}_k - \beta^* \rho \omega k + \frac{\partial}{\partial x_j} \left(\Gamma_k \frac{\partial k}{\partial x_j} \right) \quad (3)$$

$$\frac{\partial \rho \omega}{\partial t} + \frac{\partial \rho U_j \omega}{\partial x_j} = \frac{\gamma}{\nu_t} P_k - \beta \rho \omega^2 + \frac{\partial}{\partial x_j} \left(\Gamma_\omega \frac{\partial \omega}{\partial x_j} \right) + (1 - F_1) 2 \rho \sigma_{\omega 2} \frac{1}{\omega} \frac{\partial k}{\partial x_j} \frac{\partial \omega}{\partial x_j} \quad (4)$$

with

$$\Gamma_k = \mu + \frac{\mu_t}{\sigma_k}, \quad \Gamma_\omega = \mu + \frac{\mu_t}{\sigma_\omega}, \quad P_k = \tau_{ij} \frac{\partial U_i}{\partial x_j}, \quad \tilde{P}_k = \min(P_k; c_1 \epsilon), \quad \mu_t = \rho \frac{a_1 k}{\max(a_1 \omega; S \cdot F_2)} \quad (5)$$

The coefficients, ϕ of the model are function of F_1 : $\phi = F_1 \phi_1 + (1 - F_1) \phi_2$, where ϕ_1 and ϕ_2 stand for the coefficients for the $k - \omega$ and the $k - \epsilon$ model respectively:

$$\sigma_{k1} = 1.176, \quad \sigma_{\omega 1} = 2.000, \quad \kappa = 0.41, \quad \gamma_1 = 0.5532, \quad \beta_1 = 0.0750, \quad \beta^* = 0.09, \quad c_1 = 10 \quad (6)$$

$$\sigma_{k2} = 1.00, \quad \sigma_{\omega 2} = 1.168, \quad \kappa = 0.41, \quad \gamma_2 = 0.4403, \quad \beta_2 = 0.0828, \quad \beta^* = 0.09 \quad (7)$$

with

$$F_1 = \tanh \left(\min \left(\max \left(\frac{\sqrt{k}}{\beta^* \omega y}; \frac{500 \nu}{y^2 \omega} \right); \frac{4 \rho \sigma_{\omega 2} k}{CD_{k\omega} y^2} \right) \right) \quad (8)$$

$$CD_{k\omega} = \max \left(2 \rho \sigma_{\omega 2} \frac{1}{\omega} \frac{\partial k}{\partial x_j} \frac{\partial \omega}{\partial x_j}; 1.0e^{-10} \right) \quad (9)$$

$$F_2 = \tanh \left(\max \left(2 \frac{\sqrt{k}}{\beta^* \omega y}; \frac{500 \nu}{y^2 \omega} \right) \right) \quad (10)$$

$$\tau_{ij} = \mu_t \left(\frac{\partial U_i}{\partial x_j} + \frac{\partial U_j}{\partial x_i} - \frac{2}{3} \frac{\partial U_k}{\partial x_k} \right) - \frac{2}{3} \rho k \delta_{ij} \quad (11)$$

Here, the absolute value of the strain rate, S , is used in the definition of the eddy viscosity instead of the vorticity in order to increase the generality of the method beyond aerodynamic applications. The turbulent heat flux vector is modelled with the help of a turbulent diffusivity:

$$\overline{u'_i T'} = -\varepsilon_h \frac{\partial T}{\partial x_i} = -\frac{\nu_t}{Pr_t} \frac{\partial T}{\partial x_i} \quad (12)$$

with

$$Pr_t = \frac{\nu_t}{\varepsilon_h} \quad (13)$$

Finally, the temperature equation is written as:

$$\frac{\partial \rho T}{\partial t} + \frac{\partial \rho U_j T}{\partial x_j} = \frac{\partial}{\partial x_j} \left[\left(\frac{\mu}{Pr} + \frac{\mu_t}{Pr_t} \right) \frac{\partial T}{\partial x_j} \right] \quad (14)$$

The Prandtl number, Pr , is a fluid property, and the turbulent Prandtl number, Pr_t , is set to a constant value of 0.9, assuming an analogy between turbulent heat and mass transfert.

3.4.2 Lahey $k - \epsilon$

This $k - \epsilon$ model has been developed by Lahey [5] specifically for three-dimensional, four-field, turbulent, two-fluid multiphase flows. It is an extension to two-phase flows of the standard single-phase $k - \epsilon$ turbulence model. In particular, for bubbly flows only two fields are required: the continuous liquid (cl) and dispersed vapor (dv) fields. Therefore, the following turbulent equations are used:

$$\alpha_{cl} \frac{Dk_{cl}}{Dt} = \nabla \cdot \left[\alpha_{cl} \frac{v_{cl}^T}{\sigma_k} \nabla k_{cl} \right] + \alpha_{cl} [P_{cl} \varepsilon_{cl}] + \alpha_{cl} \Phi_k \quad (15)$$

$$\alpha_{cl} \frac{D\varepsilon_{cl}}{Dt} = \nabla \cdot \left[\alpha_{cl} \frac{v_{cl}^T}{\sigma_k} \nabla \varepsilon_{cl} \right] + \alpha_{cl} C_{\varepsilon 1} \frac{P_{cl} \varepsilon_{cl}}{k_{cl}} - \alpha_{cl} C_{\varepsilon 2} \frac{\varepsilon_{cl}^2}{k_{cl}} + \alpha_{cl} \Phi_k \quad (16)$$

where

$$k_{cl} = \frac{1}{2} \overline{v'_{cl} \cdot v'_{cl}} \quad (17)$$

$$\nu_{cl}^T = C_\mu \frac{k_{cl}^2}{\varepsilon_{cl}} + 0.6 D_{dv} \alpha_{dv} |\underline{v}_r| \quad (18)$$

$$\underline{v}_r = \underline{v}_{dv} - \underline{v}_{cl} \quad (19)$$

The source term for turbulent kinetic energy is:

$$\Phi_k = \frac{k_{cl}}{C_{\varepsilon 2} \varepsilon_{cl}} = C_p (1 + C_D^{4/3}) \alpha_{dv} \frac{|\underline{v}_r|^3}{D_{dv}} \quad (20)$$

where $C_p = 0.25$. Eq. (20) accounts for the velocity fluctuations induced by liquid displacement due to the relative velocity (\underline{v}_r) and the liquid eddies which may be formed behind the bubbles. Similar turbulent transport equations can be written for the dispersed phase.

3.4.3 Mixture $k - \epsilon$

The *Mixture* $k - \epsilon$ model [6] has been developed to overcome the limitations of the standard $k - \epsilon$ turbulence model in the application to dilute systems.

As the phase fraction increases, the dominance of the continuous phase on turbulence gradually diminishes as that phase becomes confined to thin interstices between dispersed phase elements. In the limit of unity dispersed phase fraction, this phase becomes continuous and its turbulence becomes the dominant/sole factor.

The *Mixture* $k - \epsilon$ model appropriately incorporate high phase regimes and reverts to the single-phase form in the extreme limits of zero and unity phase fractions.

The turbulence equations take the form:

$$\frac{\partial}{\partial t} (\rho_m k_m) + \nabla \cdot (\rho_m \tilde{U}_m k_m) = \nabla \cdot \left(\frac{\mu_m^t}{\sigma_m} \nabla k_m \right) + P_k^m - \rho_m \varepsilon_m + S_k^m \quad (21)$$

$$\frac{\partial}{\partial t} (\rho_m \varepsilon_m) + \nabla \cdot (\rho_m \tilde{U}_m \varepsilon_m) = \nabla \cdot \left(\frac{\mu_m^t}{\sigma_m} \nabla \varepsilon_m \right) + \frac{\varepsilon_m}{k_m} (C_{\varepsilon 1} P_k^m - C_{\varepsilon 2} \rho_m \varepsilon_m) + C_{\varepsilon 3} \frac{\varepsilon_m}{k_m} S_k^m \quad (22)$$

The mixture quantities (referred by the subscript m) appearing in the equations are defined by

$$\rho_m = \bar{\alpha}_c \rho_c + \bar{\alpha}_d \rho_d \quad (23)$$

The mixture properties can be related to those of the continuous and dispersed as follow

$$k_m = \left(\bar{\alpha}_c \frac{\rho_c}{\rho_m} + \bar{\alpha}_d \frac{\rho_d}{\rho_m} C_t^2 \right) k_c \quad (24)$$

$$\varepsilon_m = \left(\bar{\alpha}_c \frac{\rho_c}{\rho_m} + \bar{\alpha}_d \frac{\rho_d}{\rho_m} C_t^2 \right) \varepsilon_c \quad (25)$$

$$\tilde{U}_m = \frac{\bar{\alpha}_c \rho_c \tilde{U}_c + \bar{\alpha}_d \rho_d \tilde{U}_d C_t^2}{\bar{\alpha}_c \rho_c + \bar{\alpha}_d \rho_d C_t^2} \quad (26)$$

$$\mu_m^t = \frac{(\bar{\alpha}_c \mu_c^t + \bar{\alpha}_d \mu_d^t C_t^2) \rho_m}{\bar{\alpha}_c \rho_c + \bar{\alpha}_d \rho_d C_t^2} \quad (27)$$

$$P_k^n = \bar{\alpha}_c P_k^c + \bar{\alpha}_d P_k^d \quad (28)$$

$$S_k^m = S_k^c + S_k^d = -A_d(2\alpha_d(C_t - 1)^2 k_c + \nu_c \nabla \alpha_d \cdot \bar{U}_r) \quad (29)$$

$$\mu_d^t = C_t^2 \left(\frac{\nu_c}{\nu_d} \frac{\rho_d}{\rho_c} \right) \mu_c^t \quad (30)$$

3.5. Solver settings

The *multiphaseEulerFoam* solver enables simultaneous modelling of complex multiphase flows with different flow regimes. Usually the VOF interface capturing method is used to model the large fluid-fluid interfaces, whereas in our case the Euler multi-fluid approach is used for modelling the dispersed flow. In the Euler multi-fluid approach each phase is represented by separate set of flow equations. The multi-fluid model governing equations for compressible, isothermal flow are given by a set of mass and momentum equations for each phase i :

$$\frac{\partial \alpha_i}{\partial t} + u_i \cdot \nabla(\alpha_i) = 0 \quad (31)$$

$$\frac{\partial \rho_i \alpha_i u_i}{\partial t} + \rho_i \alpha_i u_i \cdot \nabla u_i = -\alpha_i \nabla p + \nabla \cdot (\mu_i \alpha_i \nabla u_i) + F_g + F_{D,i} + F_{st,i} \quad (32)$$

where α_i is the phase fraction, ρ_i the density, u_i the velocity each for the respective phase i and F_g is the gravitational force. The two interfacial forces are the drag force $F_{D,i}$ and the surface tension force $F_{st,i}$.

The first step is to define the properties of each compressible fluid phases with common pressure. Subsequently, the phase transport equations are solved for each individual phases and are calculated the interface properties of different phase pairs. The flow equations are solved through the use of the PIMPLE (Semi-Implicit Method for Pressure-Linked Equations) algorithm. Different sub-models are used for defining interfacial properties between each individual phase pairs for example the **dragModel**. In Table 4 and 5 are summarized the choices made.

Mathematical term	Numerical scheme
ddtSchemes	backward
gradSchemes	cellLimited Gauss linear 1
divSchemes	Gauss vanLeer
laplacianSchemes	Gauss linear limited 1
interpolationSchemes	linear
snGradSchemes	limited 1

Table 4: List of numerical schemes adopted for the different mathematical terms in the **fvSchemes** file

Table 5: List of entries adopted in the **fvSolution** file for both the air and water

Variable	Solver	Smoother	Tolerance
U, e, k, epsilon, omega	smoothSolver	symGaussSeidel	10^{-7}
p	GAMG	DIC	10^{-8}

Correctors		Relaxation factors	
alpha	1	p	0.3
PIMPLE loop	2	All equations	0.5

3.6. Phase interaction modeling

Interfacial forces between bubbles and liquid are of fundamental importance when modeling a multiphase system. They are responsible of momentum transfer between phases in the Eulerian framework. Therefore, their careful modeling is directly linked to the accuracy of the results. Several forces are acting on a bubble in a multiphase system. They are: virtual mass force, drag, lift, turbulent dispersion and wall lubrication forces. In the next paragraphs a brief description for each force is given.

3.6.1 Virtual mass force

The virtual mass force describes resistance to relative acceleration. It occurs when a secondary phase accelerates relative to the primary phase. The inertia of the primary-phase mass encountered by the accelerating particles (or droplets or bubbles) exerts a "virtual mass force" on the particles. Its formulation is fairly simple and it is given in equation 33

$$\begin{aligned}\vec{F}_{VM} &= C_{VM} \alpha_p \rho_q \left(\frac{d_q \vec{v}_q}{dt} - \frac{d_p \vec{v}_p}{dt} \right) \\ C_{VM} &= 0.5\end{aligned}\tag{33}$$

3.6.2 Drag force

This force model is used to describe the resistance acting on the bubble due to relative motion in the fluid (primary phase). In this work the simulations were performed using the drag model developed by Ishii and Zuber in [7]. This is a very complete drag model that accounts for bubble deformation. In fact, depending on Eötvös number, a rising bubble can have a spherical shape, an elliptic one or deforming to a spherical cap. Ishii and Zuber's model models the drag coefficient as:

$$\begin{aligned}C_D &= \max(C_{D, \text{sphere}}, \min(C_{D, \text{ellipse}}, C_{D, \text{cap}})) \\ C_{D, \text{sphere}} &= \frac{24}{Re_P} (1 + 0.1 Re_P^{0.75}) \\ C_{D, \text{ellipse}} &= \frac{2}{3} \sqrt{Eo} \\ C_{D, \text{cap}} &= \frac{8}{3}\end{aligned}\tag{34}$$

3.6.3 Lift force

The lift force describes migration of bubble in shear flow acting on a particle mainly due to velocity gradients in the primary phase flow field. The expression of the lift force on a secondary phase p in a primary phase q is given by:

$$\vec{F}_{lift} = -C_l \rho_q \alpha_p \left(\vec{v}_q - \vec{v}_p \right) \times \left(\nabla \times \vec{v}_q \right)\tag{35}$$

In this work two main lift models were tested: Moraga's [8] and Tomiyama's [9].

The first one was developed for solid spherical particles but can be employed also for spherical bubbles. In this model two contributions to the lift force are accounted for: the classical aerodynamic one and the vorticity-induced lift. Its formulation is given in equation 36.

$$C_l = - \left(0.12 - 0.2e^{-(\varphi/3.6) \times 10^{-5}} \right) e^{(\varphi/3) \times 10^{-7}} \quad 6000 < \varphi < 5 \times 10^7$$

where $\varphi = \text{Re}_p \text{Re}_\omega$ and

$$\text{Re}_p = \frac{\rho_q |\vec{V}_q - \vec{V}_p| d_p}{\mu_q} \quad (36)$$

$$\text{Re}_\omega = \frac{\rho_q |\nabla \times \vec{V}_q| d_p^2}{\mu_q}$$

Tomiyama's models, instead, can be applied also to deformed bubbles. Its main feature is prediction of the cross-over point in bubble size at which particle distortion causes a reversal in the sign of the lift force. Bubbles with a diameter larger than about 5.8mm have negative lift coefficient and move towards the center of the column while small ones move towards the walls. Equation 37 shows the fundamental equations of this model.

$$C_L = \begin{cases} \min [0.288 \tanh (0.121 \text{Re}_P), f(Eo_\perp)] & Eo_\perp < 4 \\ f(Eo_\perp) & 4 < Eo_\perp < 10 \\ -0.27 & 10 < Eo_\perp \end{cases} \quad \text{for} \quad (37)$$

$$f(Eo_\perp) = 0.00105 Eo_\perp^3 - 0.0159 Eo_\perp^2 - 0.0204 Eo_\perp + 0.474$$

$$Eo_\perp = \frac{g(\rho_C - \rho_D) d_\perp^2}{\sigma}$$

3.6.4 Turbulent dispersion

This force accounts for the interphase turbulent momentum transfer. The turbulent dispersion force acts as a turbulent diffusion in dispersed flows. The model considered in this report and the ones by Lopez de Bertodano [10] and Burns [11]. This formulation is reported in equations 38 and 39 respectively.

$$\vec{F}_{td,q} = -\vec{F}_{td,p} = C_{TD} \rho_q k_q \nabla \alpha_p \quad (38)$$

$$\vec{F}_{td,q} = -\vec{F}_{td,p} = C_{TD} K_{pq} \frac{D_q}{\sigma_{pq}} \left(\frac{\nabla \alpha_p}{\alpha_p} - \frac{\nabla \alpha_q}{\alpha_q} \right) \quad (39)$$

3.6.5 Wall lubrication

It describes migration of bubble away from the walls due to the presence of the walls themselves. This results in the dispersed phase concentrating in a region near but not adjacent to the walls. The general expression of the wall lubrication force acting on a secondary phase p in a primary phase q is given by:

$$\vec{F}_{wl} = C_{wl} \rho_q \alpha_p \left| (\vec{v}_q - \vec{v}_p)_\parallel \right|^2 \vec{n}_w \quad (40)$$

where C_{wl} is the wall lubrication coefficient and \vec{n}_w the unit normal to the wall.

In this work two different models between the ones already available in openFOAM were considered: Antal's [12] and Frank's one [13].

The first one computes the wall lubrication coefficient as

$$C_{wl} = \max \left(0, \frac{C_{w1}}{d_b} + \frac{C_{w2}}{y_w} \right) \quad (41)$$

where C_{w1} and C_{w2} are non-dimensional coefficients and y_w is the distance to the nearest wall.

Frank's model, instead, computes C_{wl} as

$$C_{wl} = C_w \max \left(0, \frac{1}{C_{wd}} \cdot \frac{1 - \frac{y_w}{C_{wd} d_b}}{y_w \left(\frac{y_w}{C_w d_b} \right)^{m-1}} \right) \quad (42)$$

where C_{wd} , C_{wc} and m are calibration coefficients.

4. Results and Discussion

In this section the results of the present work are presented and commented. Each subsection represents the sensitivity analysis on some parameters which may or may not influence the numerical results. The analysis performed aim at evaluating the sensitivity of the cfd results on the mesh, timestep and each multiphase force in this order.

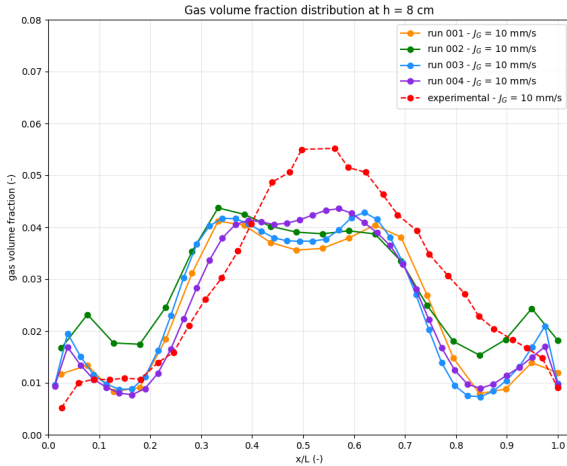
4.1. CFD methodology

All the simulations are three-dimensional and time-dependent. The solution was initialized with constant pressure distribution at P_{atm} and the bubble column was filled with water. The simulated time was 90 seconds for each case. Results were averaged from 30 s to the end of the simulations in order to obtain the averaged field in terms of velocity, pressure and void fraction distribution for both phases. In particular, the air void fraction was sampled on two horizontal surfaces at 8 cm and 63 cm from the inlet surface in order to compare the numerical results to the experimental ones.

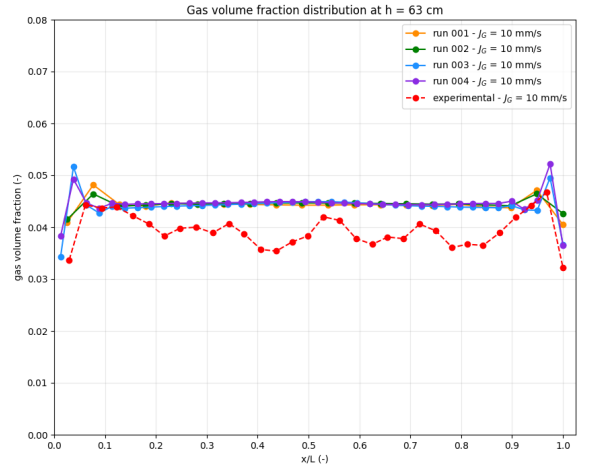
4.2. Mesh sensitivity

		N_x	N_y	N_z	Experimental holdup	Numerical hold up
run001	Mesh A	20	200	4	0.03501	
run002	Mesh B	20	200	8	0.03501	
run003	Mesh C	40	200	8	0.03501	
run004	Mesh D	40	400	8	0.03501	

Table 7: Meshes



(a) $h = 8$ cm



(b) $h = 63$ cm

Figure 3: Gas volume fraction horizontal distribution at different heights for different meshes

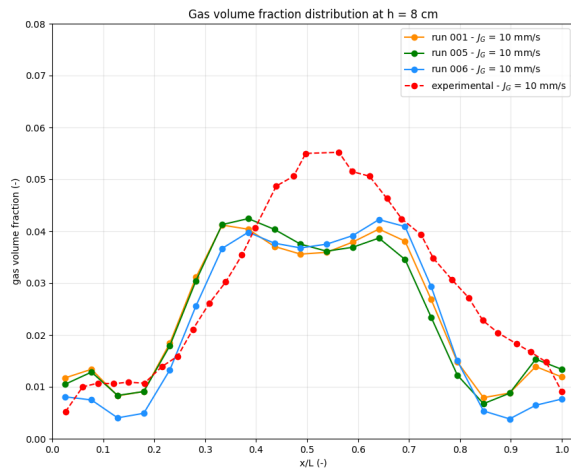
	$J_{in}[mm/s]$	Mesh	Time step	Turbulence model	Drag model	Lift model	Turbulent dispersion model	Wall lubrication model
run001	10	A	0.005	kOmegaSSTsato	IshiiZuber	Tomiyama	None	None
run002	10	B	0.005	kOmegaSSTsato	IshiiZuber	Tomiyama	None	None
run003	10	C	0.005	kOmegaSSTsato	IshiiZuber	Tomiyama	None	None
run004	10	D	0.005	kOmegaSSTsato	IshiiZuber	Tomiyama	None	None
run005	10	A	0.010	kOmegaSSTsato	IshiiZuber	Tomiyama	None	None
run006	10	A	0.0025	kOmegaSSTsato	IshiiZuber	Tomiyama	None	None
run007	10	A	0.005	LaheyKEpsilon	IshiiZuber	Tomiyama	None	None
run008	10	A	0.005	mixtureKEpsilon	IshiiZuber	Tomiyama	None	None
run009	10	A	0.005	kOmegaSSTsato	IshiiZuber	None	None	None
run010	10	A	0.005	kOmegaSSTsato	IshiiZuber	Moraga	None	None
run011	10	A	0.005	kOmegaSSTsato	IshiiZuber	Tomiyama	Burns	None
run012	10	A	0.005	kOmegaSSTsato	IshiiZuber	Tomiyama	LopezDeBertodano	None
run013	10	A	0.005	kOmegaSSTsato	IshiiZuber	Tomiyama	Burns	Antal
run014	10	A	0.005	kOmegaSSTsato	IshiiZuber	Tomiyama	Burns	Frank
run015	8	A	0.005	kOmegaSSTsato	IshiiZuber	Tomiyama	Burns	Antal
run016	6	A	0.005	kOmegaSSTsato	IshiiZuber	Tomiyama	Burns	Antal

Table 6: Runs performed

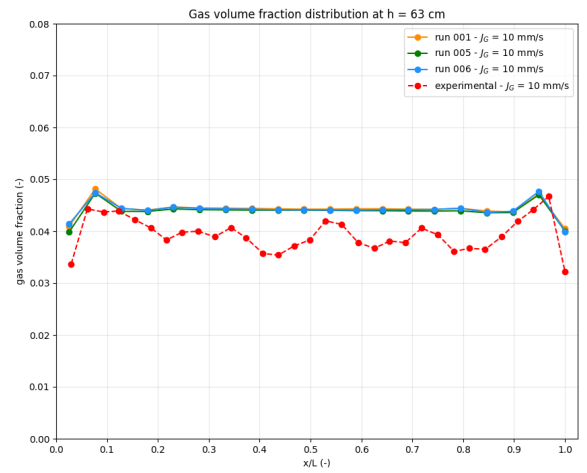
4.3. Time sensitivity

	Δt	Experimental holdup	Numerical hold up
run006	0.0025	0.03501	
run001	0.005	0.03501	
run005	0.010	0.03501	

Table 8: Time steps



(a) $h = 8$ cm



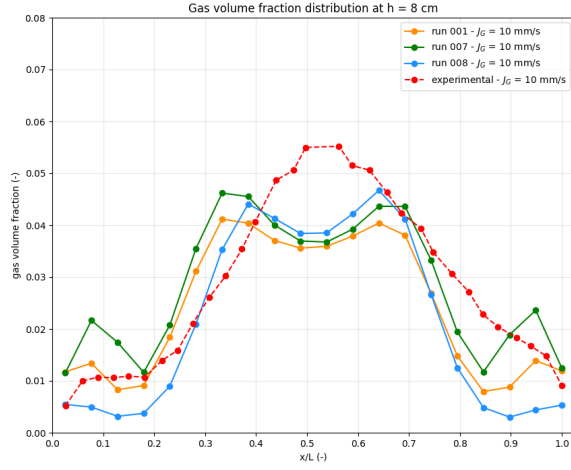
(b) $h = 63$ cm

Figure 4: Gas volume fraction horizontal distribution at different heights for different time steps

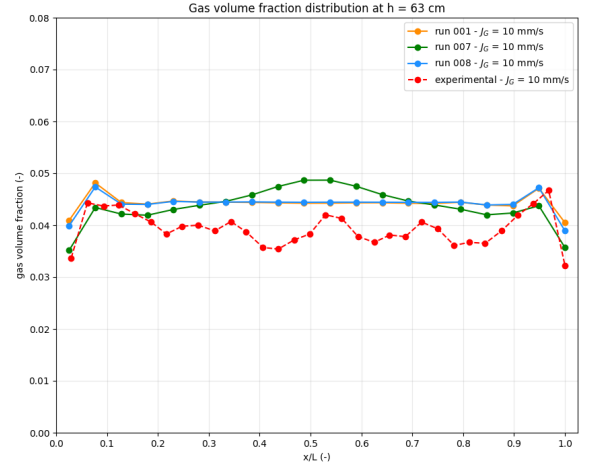
4.4. Turbulence models

	Turbulence model	Experimental holdup	Numerical hold up
run001	kOmegaSSTsato	0.03501	
run007	LaheyKEpsilon	0.03501	
run008	mixtureKEpsilon	0.03501	

Table 9: Turbulence models



(a) $h = 8$ cm



(b) $h = 63$ cm

Figure 5: Gas volume fraction horizontal distribution at different heights for different turbulence models

4.5. Drag models

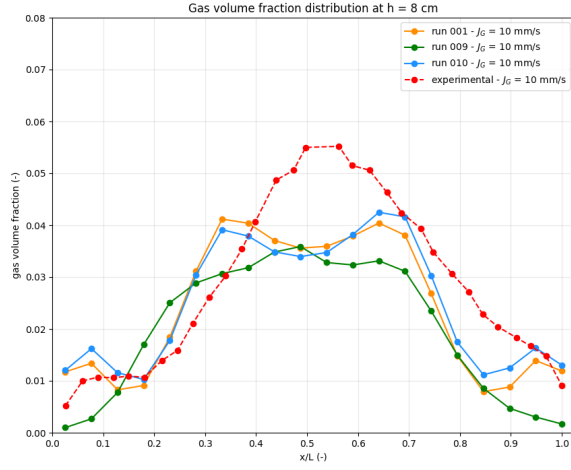
Drag model	Experimental holdup	Numerical hold up
all runs	0.03501	

Table 10: Drag models

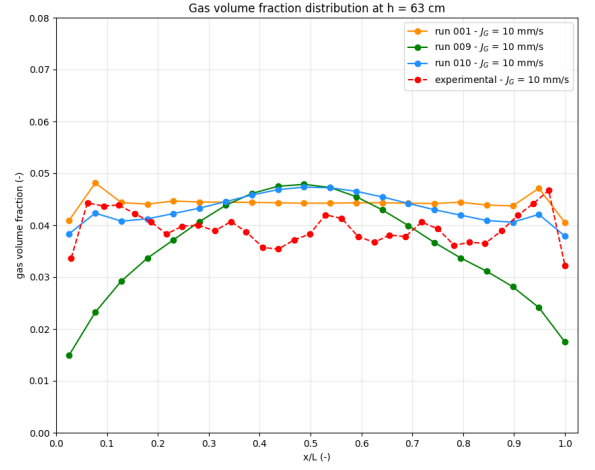
4.6. Lift models

	Lift model	Experimental holdup	Numerical hold up
run009	None	0.03501	
run001	Tomiyama	0.03501	
run010	Moraga	0.03501	

Table 11: Lift models



(a) $h = 8$ cm



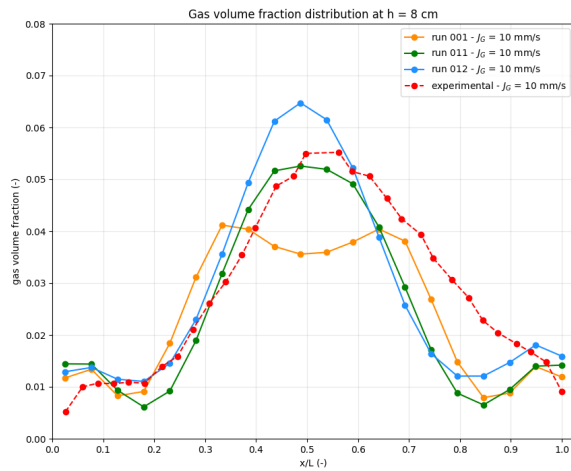
(b) $h = 63$ cm

Figure 6: Gas volume fraction horizontal distribution at different heights for different lift models

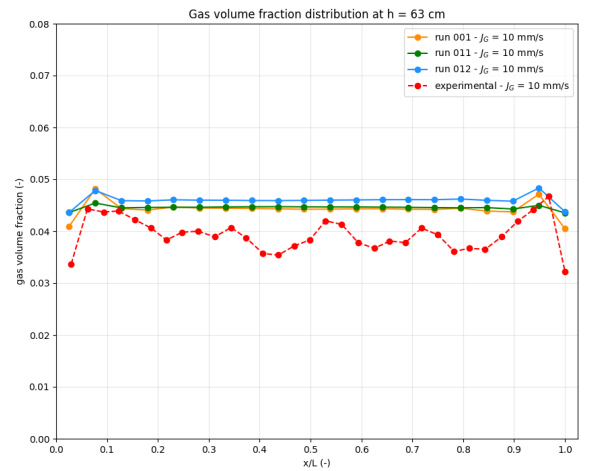
4.7. Turbulent dispersion models

Turbulent dispersion model		Experimental holdup	Numerical hold up
run001	None	0.03501	
run011	Burns	0.03501	
run012	LopezDeBertodanone	0.03501	

Table 12: Turbulent dispersion models



(a) $h = 8$ cm



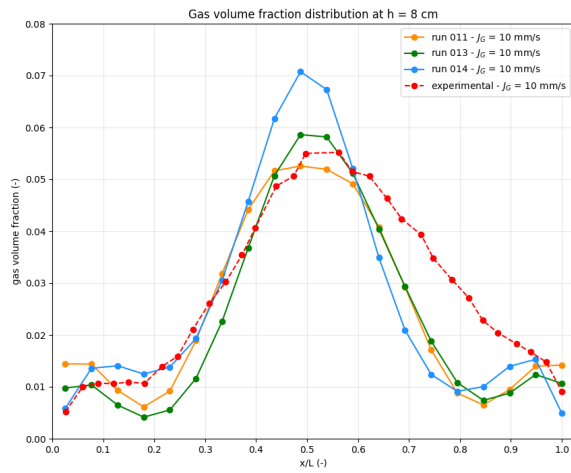
(b) $h = 63$ cm

Figure 7: Gas volume fraction horizontal distribution at different heights for different turbulent dispersion models

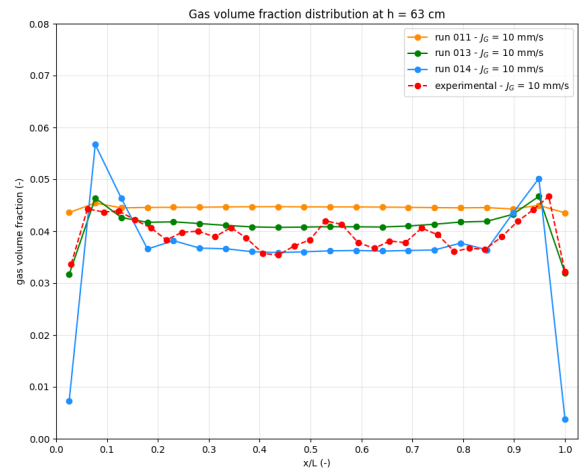
4.8. Wall lubrication models

Wall lubrication model		Experimental holdup	Numerical hold up
run001	None	0.03501	
run013	Antal	0.03501	
run014	Frank	0.03501	

Table 13: Wall lubrication models



(a) $h = 8$ cm



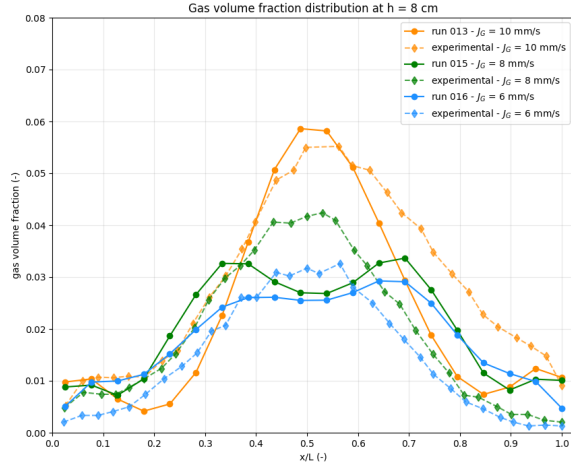
(b) $h = 63$ cm

Figure 8: Gas volume fraction horizontal distribution at different heights for different wall lubrication models

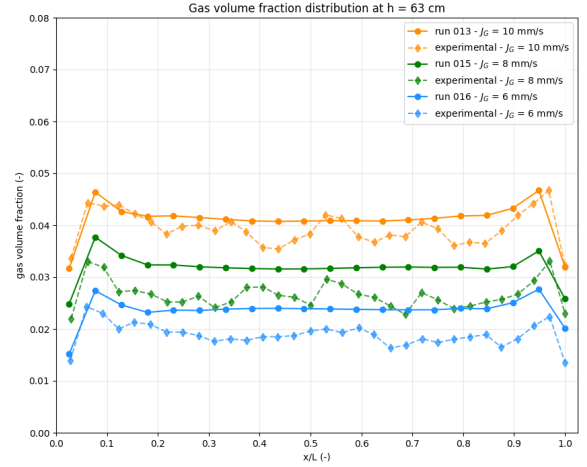
4.9. Inflow velocity

	$J_{in}[mm/s]$	Experimental holdup	Numerical hold up
run013	10	0.03501	
run015	8	0.02808	
run016	6	0.02042	

Table 14: Inflow velocities



(a) $h = 8 \text{ cm}$



(b) $h = 63 \text{ cm}$

Figure 9: Gas volume fraction horizontal distribution at different heights for different inflow velocities

References

- [1] OpenFOAM®-foundation. Openfoam version 9.0, 2021. URL <https://openfoam.org>.
- [2] Eckhard Krepper, Brahma Nanda Reddy Vanga, Alexandr Zaruba, Horst-Michael Prasser, and Martin A Lopez de Bertodano. Experimental and numerical studies of void fraction distribution in rectangular bubble columns. *Nuclear engineering and design*, 237(4):399–408, 2007.
- [3] ANSYS Fluent. Fluent 2021 R2 user’s guide. *Ansys Fluent Inc*, 2021.
- [4] Florian Menter and Thomas Esch. Elements of industrial heat transfer predictions. *16th Brazilian Congress of Mechanical Engineering (COBEM)*, 20:117–127, 2001.
- [5] Richard T. Lahey Jr. The simulation of multidimensional multiphase flows. *Nuclear Engineering and Design*, 235:1043–1060, 2005.
- [6] A. Behzadi, R.I Issa, and H. Rusche. Modelling of dispersed bubble and droplet flow at high phase fractions. *Chemical Engineering Science*, 59:759–770, 2004.
- [7] Mamoru Ishii and Novak Zuber. Drag coefficient and relative velocity in bubbly, droplet or particulate flows. *AIChE journal*, 25(5):843–855, 1979.
- [8] FJ Moraga, FJ Bonetto, and RT Lahey. Lateral forces on spheres in turbulent uniform shear flow. *International Journal of Multiphase Flow*, 25(6-7):1321–1372, 1999.
- [9] Akio Tomiyama, Hidesada Tamai, Iztok Zun, and Shigeo Hosokawa. Transverse migration of single bubbles in simple shear flows. *Chemical Engineering Science*, 57(11):1849–1858, 2002.
- [10] Martin Aurelio Lopez de Bertodano. *Turbulent bubbly two-phase flow in a triangular duct*. PhD thesis, Rensselaer Polytechnic Institute, 1992.
- [11] Alan D Burns, Thomas Frank, Ian Hamill, Jun-Mei Shi, et al. The favre averaged drag model for turbulent dispersion in eulerian multi-phase flows. In *5th international conference on multiphase flow, ICMF*, volume 4, pages 1–17. ICMF, 2004.
- [12] SP Antal, RT Lahey Jr, and JE Flaherty. Analysis of phase distribution in fully developed laminar bubbly two-phase flow. *International journal of multiphase flow*, 17(5):635–652, 1991.
- [13] Thomas Frank. Advances in computational fluid dynamics (cfd) of 3-dimensional gas-liquid multiphase flows. In *NAFEMS Seminar: Simulation of Complex Flows (CFD)–Applications and Trends, Wiesbaden, Germany, Citeseer*, pages 1–18, 2005.

A. Appendix A: fvModels source code for degassing boundary conditions

```
/*-----*- C++ -*-----*/
| ===== |
| \ \ / F i e l d | OpenFOAM: The Open Source CFD Toolbox |
| \ \ / O p e r a t i o n | Version: 3.0.0 |
| \ \ / A n d | Web: www.OpenFOAM.org |
| \ \ / M a n i p u l a t i o n |
|-----*/
FoamFile
{
    version      2.0;
    format       ascii;
    class        dictionary;
    location     "constant";
    object       fvOptions;
}
// * * * * *

degassingMassSource
{
    type          coded;
    active        yes;
    selectionMode all;
    field         thermo:rho.air;

    name          degassingMassSource;
    patches       (outlet);
    rhoName       thermo:rho.air;
    alphaName     alpha.air;

    codeInclude
    #{
        #include "fvm.H"
    #};

    codeAddRhoSup
    #{

        Info << "**codeAddSup**" << endl;

        // Get the names of the patches on which to apply the degassing forces
        DynamicList<word, 1, 0> patches;
        coeffs().lookup("patches") >> patches;

        // Get the required fields
        const word rhoName = coeffs().lookup("rhoName");
        const volScalarField& rhoAir = mesh().lookupObject<volScalarField>(rhoName);
        const word alphaName = coeffs().lookup("alphaName");
        const volScalarField& alphaAir = mesh().lookupObject<volScalarField>(alphaName);

        // Get the timestep
        const scalar deltaT = mesh().time().deltaT().value();

        // Create degassing mass source coefficient and initialize to zero
        volScalarField degassingMassSourceCoeff
        (
```

```

        IOobject
        (
            "degassingMassSourceCoeff",
            mesh().time().timeName(),
            mesh(),
            IOobject::NO_READ,
            IOobject::AUTO_WRITE
        ),
        mesh(),
        dimensionedScalar("degassingMassSourceCoeff", dimless/dimTime, 0.0)
    );

    // Compute the degassing mass source coefficient for each cell adjacent to the
    // selected patches
    forAll(patches, iPatch)
    {
        // Get the boundary patch
        const fvPatch& patch = mesh().boundary()[patches[iPatch]];

        // Loop through each boundary face and compute degassing force coefficient in
        // adjacent cell
        forAll(patch, iFace)
        {
            label iCell = patch.faceCells()[iFace];
            degassingMassSourceCoeff[iCell] = -alphaAir[iCell]/deltaT;
        }
    }

    // Add the degassing force term
    eqn += fvm::Sp(degassingMassSourceCoeff, rhoAir);
#};

codeOptions
#{
-I$(LIB_SRC)/finiteVolume/lnInclude \
-I$(LIB_SRC)/meshTools/lnInclude
#};
}

degassingForce
{
    type            coded;
    active          yes;
    selectionMode    all;
    field            U.air;
    name            degassingForce;
    patches          (outlet);
    rhoName          thermo:rho.air;
    alphaName        alpha.air;
    UName            U.air;

    codeInclude
    #{
        #include "fvm.H"
    #};

    codeAddRhoSup
    #{

```

```

// Get the names of the patches on which to apply the degassing forces
DynamicList<word, 1, 0> patches;
coeffs().lookup("patches") >> patches;

// Get the required fields
const word rhoName = coeffs().lookup("rhoName");
const volScalarField& rhoAir = mesh().lookupObject<volScalarField>(rhoName);
const word alphaName = coeffs().lookup("alphaName");
const volScalarField& alphaAir = mesh().lookupObject<volScalarField>(alphaName);
const word UName = coeffs().lookup("UName");
const volVectorField& UAir = mesh().lookupObject<volVectorField>(UName);

// Get the timestep
const scalar deltaT = mesh().time().deltaT().value();

// Create degassing force coefficient and initialize to zero
volScalarField degassingForceCoeff
(
    IOobject
    (
        "degassingForceCoeff",
        mesh().time().timeName(),
        mesh(),
        IOobject::NO_READ,
        IOobject::AUTO_WRITE
    ),
    mesh(),
    dimensionedScalar("degassingForceCoeff", dimDensity/dimTime, 0.0)
);

// Compute the degassing force coefficient for each cell adjacent to the selected
patches
forAll(patches, iPatch)
{
    // Get the boundary patch
    const fvPatch& patch = mesh().boundary()[patches[iPatch]];

    // Loop through each boundary face and compute degassing force coefficient in
adjacent cell
    forAll(patch, iFace)
    {
        label iCell = patch.faceCells()[iFace];
        degassingForceCoeff[iCell] = -rhoAir[iCell]*alphaAir[iCell]/deltaT;
    }
}

// Add the degassing force term
eqn += fvm::Sp(degassingForceCoeff, UAir);
#};

codeOptions
#{
-I$(LIB_SRC)/finiteVolume/lnInclude \
-I$(LIB_SRC)/meshTools/lnInclude
#};
}

// *****

```

Listing 1: fvModels source code